AIChE

Experimental and CFD Studies of Fluid Dynamic Gauging in Annular Flows

T. Gu, Y. M. J. Chew, W. R. Paterson, and D. I. Wilson
Dept. of Chemical Engineering and Biotechnology, University of Cambridge,
New Museums Site, Cambridge CB2 3RA, U.K.

DOI 10.1002/aic.11789
Published online June 22, 2009 in Wiley InterScience (www.interscience.wiley.com).

Fluid dynamic gauging has been applied for the first time to measurements on a curved surface, specifically the inner convex surface of an annulus. Two hydraulic cases were examined: (i) the quasi-static case, where there is no flow in the annulus, other than the flow imposed by the working action of the gauge and (ii) the turbulent case, where there is additionally a forced advective flow in the turbulent regime (14,000 $<$ $Re_{annulus}$ $<$ 32,000). The nozzle clearance–flow rate characteristics resembled those reported previously for flat geometries, with one exception; at small clearance values (0 $<$ h/d_t $<$ 0.1), flow rate was found to be independent of clearance because of a leakage flow arising from the curvature of the surface. The experimental results for the quasi-static case showed very good agreement with simulations of the configuration using computational fluid dynamics (CFD). The agreement indicates that the technique may be used not only for measuring the thickness of deposits on curved surfaces, but also for measuring their strength. CFD simulation of the turbulent case was not attempted, but the experimental results imply that the technique could be used reliably as a real-time in situ thickness sensor for this scenario, which is often employed in laboratory fouling studies.
AIChE J, 55: 1937–1947, 2009
Keywords: CFD, fluid dynamic gauging, fouling, concentric annulus, surface stress distribution

Introduction

The current high costs of energy means that energy recovery, e.g., via heat exchanger networks, should be exploited where possible. Fouling, the attachment and accumulation of material from process streams on heat transfer (and other) surfaces, is therefore highly undesirable as it reduces heat transfer and hydraulic efficiencies. The associated step of cleaning incurs added costs and problems in disposal of waste streams.[1] Long-term mitigation of fouling and effective cleaning require an understanding of the mechanisms involved in deposition and cleaning. Experimental studies are often required to develop this knowledge.

Correspondence concerning this article should be addressed to Y. M. J. Chew at ymjc2@cam.ac.uk.

The thickness or depth of a fouling layer is a key variable but its measurement can be difficult to effect accurately, in situ, noninvasively, and quickly. One method that has been developed to measure the thickness of foulants immersed in a liquid environment in situ is the fluid dynamic gauging (FDG) technique.[2] The technique works by withdrawing liquid through a nozzle that is located near a deposit surface; the clearance between the nozzle and the surface is calculated from the measured liquid flow rate, as explained later. Measurements are performed on fouled and clean surfaces, and the deposit thickness is calculated by difference. Tuladhar et al.[2] developed the technique for studying surface layers on flat surfaces for the case where the bulk liquid was not moving, save for the flow imposed by the working action of the gauge; we label this "quasi-static FDG." This mode has been used successfully to study the fouling and cleaning of a diverse range of foulant materials and surfaces.[3]

Table 1. Examples of Recent Fouling Tests Employing Annular Flow Cells

Reference	Device	Dimensions (mm)	Type of Fouling	Fluid	$Re_{annulus}$
Turbulent flows					
Bennett et al.[6]	HTFU	$D_h = 2.77$	Chemical reaction	Different crude oils	~100,000
Oufer[7]	HTFU	$D_o = 19.6$ $D_i = 9.5$	Chemical reaction	Styrene dissolved in heptane	11,000–29,000
Chen et al.[8]		$D_o = 22$ $D_i = 16$	Crystallization	Hard water	4,000–12,000
Knudsen and Hays[9]	PFRU	$D_o = 19.6$ $D_i = 9.5$	Crystallization	Cooling tower water (containing Ca, Mg, and phosphate corrosion inhibitors)	Turbulent
Augustin and Bohnet[10]		$D_o = 40$ $D_i = 25$	Crystallization	Aqueous calcium phosphate	11,800–17,800
Toma et al.[11]		Not given	Paraffin (wax)	Paraffin and naphthenic hydrocarbons	5,540–11,100
Hays et al.[12]		$12.7 < D_h < 19.05$	Biofouling	Aqueous *Pseudomonas aerigenosa*, a known slime-forming aerobic bacterium	20,300–30,500
Laminar and transitional flows					
Bansal et al.[13]		$D_h = 7$	Chemical reaction	Milk solutions	80–163
Isogai et al.[14]	HLPS	$D_o = 4.35$ $D_i = 3.25$	Chemical reaction	Organic carbonate	~1,600
Bode et al.[15]		$D_o = 25$ $D_i = 12.5$	Chemical reaction	Whey protein concentrate solutions	1250
Watkinson[16]	PFRU	$D_o = 15.85$ $D_i = 10.7$	Chemical reaction	Three crude oils	PFRU: 1,100–5,600
	HLPS	$D_o = 4$ $D_i = 3$			HLPS: 0.3–2
Tijing et al.[17]		$D_o = 25$ $D_i = 15.86$	Crystallization	Hard water (containing $CaCO_3$)	2,700–7,300

HTFU, High Temperature Fouling Unit, by HTRI (Heat Transfer Research Inc., USA); PFRU, Portable Fouling Research Unit, by HTRI; HLPS, hot liquid process simulator, Alcor Petroleum Instruments, USA.

FDG can also be applied to monitor the growth and removal of whey protein fouling layers on a flat surface exposed to an imposed bulk flow of liquid in a duct of square cross section[4,5] (termed ''flow FDG'') with a precision in thickness measurement of better than ± 10 μm. The success of their experiments confirmed that FDG is a simple and reliable sensor for measuring thickness of soft layers immersed in a flowing liquid in situ and in real time, with a minimum knowledge of the nature of the layer. The present work describes the first applications of dynamic gauging to a curved surface, specifically the inner convex surface of an annular duct. To test our ability to determine the clearance between the nozzle and a curved surface, our experiments are not performed on a soft fouling layer, but instead directly on a smooth, rigid, metal surface.

Annular configurations are often employed in fouling tests. The active surface is usually that of the inner cylinder, as the flow pattern is well understood and the foulant layer can be viewed in situ during deposition (for the case of a clear liquid and a transparent outer cylinder), and is readily accessible for analysis or inspection after testing. Examples of previous work are summarized in Table 1. The experimental apparatus employed in this work is geometrically similar to an annular test cell being constructed at Imperial College London, which will be operating at 280°C and 3 MPa under turbulent flow conditions, as part of an investigation of refinery crude oil fouling in preheat train heat exchangers.

The mechanism of FDG operation in a concentric annulus is illustrated in Figure 1. A nozzle is located near to, but not touching, the bare substrate surface, or the surface of a

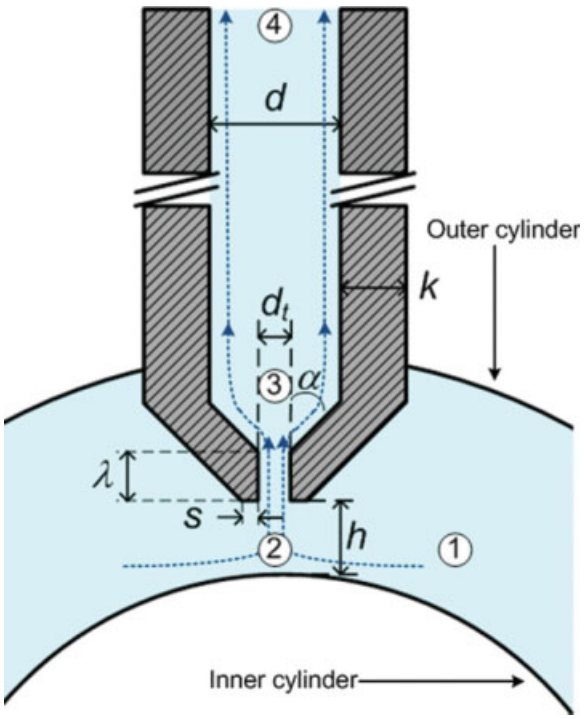

Figure 1. Schematic of fluid dynamic gauge.

d, tube i.d.; d_t, nozzle throat i.d.; *h*, clearance from surface; *k*, thickness of gauging tube; *s*, lip width; λ, length of nozzle lip; α, nozzle angle. Numbers refer to flow stations. Flow lines indicate approximate fluid flow path. [Color figure can be viewed in the online issue, which is available at www.interscience.wiley.com.]

fouling deposit immersed in liquid. A pressure difference is applied across the nozzle such that liquid is sucked into the nozzle and discharged externally; the flow rate and pressure difference are measured. The flow rate, m, is expected to be uniquely related to the distance between the nozzle and the surface, the clearance, h. For a given pressure driving force, measurements of m allow h to be calculated, and changes in h can be related to the increase (fouling) or decrease (cleaning) of deposit thickness. The main limitation is that the surface of the foulant should be sufficiently stiff that it does not change shape materially during the measurement. The gauge is operated so that its internal flow is in the laminar regime.

For design purposes, the flow behavior can be quantified in terms of a discharge coefficient, C_d. This dimensionless parameter accounts for the energy losses due to the flow near the nozzle entrance, defined as the ratio of the actual to ideal mass flow rate through the nozzle, viz.

$$C_d = \frac{m_{actual}}{m_{ideal}} = \frac{m}{\frac{\pi d_1^2}{4}\sqrt{2\rho\Delta p_{13}}} \quad (1)$$

where

$$\Delta p_{13} = \Delta p_{14} - \Delta p_{34} = \rho g H + p_s - \frac{128}{\pi}\frac{l_{eff}}{d^4}\frac{\mu}{\rho}m \quad \text{for the turbulent flow experiment} \quad (2)$$

Subscripts 1, 3, and 4 refer to various locations in the system shown in Figure 1. The static pressure (near the nozzle inlet) in the annulus, p_s, is associated with the flow in the annulus. Note that $p_s = 0$ for the quasi-static FDG case. H is the hydrostatic head, and l_{eff} is the effective length of the tube, allowing for all frictional losses in the tube.

This article presents experimental results for two different operating cases: quasi-static FDG and flow FDG, where the bulk liquid is in the turbulent regime. Experiments for the quasi-static case approximate experiments using a cold finger apparatus, where the thickness of deposit can be measured on the convex cylindrical surface.[18] The flow pattern in the quasi-static case can be modeled using computational fluid dynamics (CFD), allowing the stresses imposed on the gauged surface to be quantified and hence the forces required to remove the foulant estimated. Gu et al.[19] reported CFD simulations for the duct flow FDG configuration employed by Tuladhar et al.[4] The CFD results showed excellent agreement with experimental data for Reynolds numbers in the duct up to 930. They reported difficulties in convergence for their code at higher Reynolds numbers, which is associated with the flow approaching the transition region. Simulation of duct flow FDG in the turbulent regime, with the flow within the gauge being in the laminar regime, represents a considerable computational challenge and is not attempted here; rather, CFD simulations similar to those reported by Gu et al.[19] are presented for the quasi-static case—corresponding to gauging the fouled surface when there is no bulk flow. Experimental data alone are presented for flow FDG when the bulk flow is in the turbulent regime, corresponding to the typical flow conditions in a heat exchanger, thus being of particular interest to the industrial applications connected to this investigation.

Experimental

Quasi-static

Experiments on quasi-static FDG flows were performed using a concentric annulus held vertically (Figure 2). The outer tube (i.d. 35.1 mm) was constructed from acrylic for visualization purposes, while a length of standard stainless steel 316 rod was used for the inner tube (o.d. 21.3 mm), to ensure a stiff surface; early trials using an acrylic inner tube experienced sufficient vibration to impair the measurements. The hydraulic diameter of the annulus, D_h, defined as four times the area for flow divided by the wetted perimeter, is 13.8 mm. Concentricity was maintained using three metal locating pins at the inlet and outlet of the annulus. Constant hydrostatic heads, H = 640 mm and 540 mm, were maintained via a water refill at the top of the test section, as illustrated in Figure 2. The working fluid was water at room temperature (approximately 20°C).

The gauging nozzle was fabricated from stainless steel with dimensions: d_t = 1 mm, d = 4 mm, k = 2 mm, s = 0.5 mm, α = 45° and λ = 1.5 mm (Figure 1). It was moved backwards or forwards horizontally, normal to the inner tube, through a seal, using a micrometer. These two operating modes are referred to as "nozzle retreating" and "nozzle advancing." The micrometer also indicated the distance between the surface of the inner tube and the tip of the nozzle, h. The discharge gauging flow was measured using

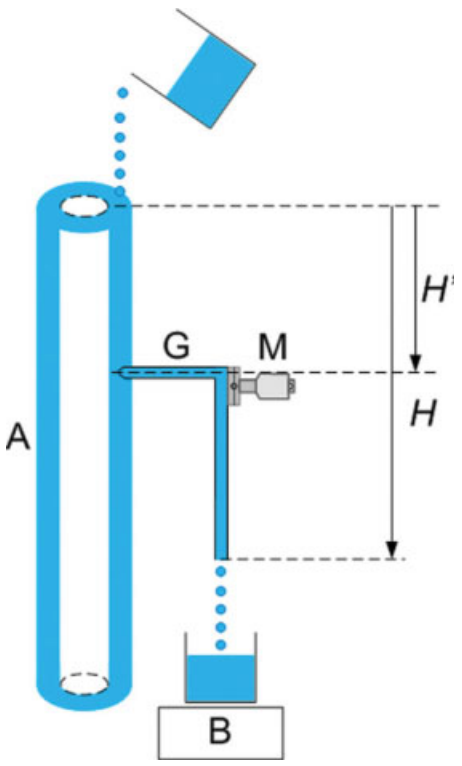

Figure 2. Schematic of quasi-static flow apparatus, where the only substantial flow is the suction flow into the nozzle.

A, annular test section; B, electronic balance; G, gauging tube; H, hydrostatic head; H', height of liquid above the gauge; M, micrometer. [Color figure can be viewed in the online issue, which is available at www.interscience.wiley.com.]

an electronic balance (accuracy ± 0.05 g). The gauging nozzle was connected to a tube of true length, $l = 525$ mm, with the other end open to the atmosphere. The value of the tube effective length, l_{eff}, used to account for frictional losses along the tube, fittings and in the bend, was estimated from

$$l_{eff} = l + K\left(\frac{\rho}{\mu}\frac{d^2}{64}\right)v_{tube} \quad (3)$$

where μ is the dynamic viscosity of the fluid, d is the tube i.d., and v_{tube} is the mean velocity in the tube. K is the loss coefficient and is a function of the coefficient of hydraulic friction of the bend, the angle of the bend, and the ratio of the radius of the bend over the internal diameter of the tube.[20] The derivation of Eq. (3) and the equation describing K can be found in the Appendix. It was not possible to find l_{eff} by experimental calibration due to the arrangement of the tube.

Flow FDG

The flow loop for flow FDG case is shown schematically in Figure 3 and is in essence an extended version of the quasi-static apparatus, using the same annular test section. The length of the annular test section, L, was 1000 mm, to ensure fully developed flow at the gauging position located 750 mm from the entry ($55D_h$). For fully developed turbulent flow, $10D_h$ is generally deemed sufficient.[6] However, statistically fully developed turbulent flow, with no significant variation in flow characteristics axially, may be achieved only after a length of $50D_h$.[21] Water flowed upwards through the annulus, with mean velocity in the range 1.0–2.3 m/s (corresponding to Reynolds numbers of 14,200–31,300, where $Re_{annulus}$ is defined in terms of D_h). The gauging nozzle, shown in Figure 1, was operated in both advancing and retreating modes at a given flow rate through the annulus. Two pressures are responsible for driving the gauging flow. The first is the suction pressure caused by the hydrostatic head, H, which was maintained constant at 405 mm (equivalent to 3970 Pa). The second is the static gauge pressure, p_s, associated with the annular flow. This latter pressure was measured using a pressure sensor (accuracy ± 34 Pa), located 750 mm from the inlet of the annulus, diametrically opposite the gauging nozzle. The measured p_s values ranged from 19,600 Pa (at $Re_{annulus} = 14{,}200$) to 42,000 Pa ($Re_{annulus} = 31{,}300$).

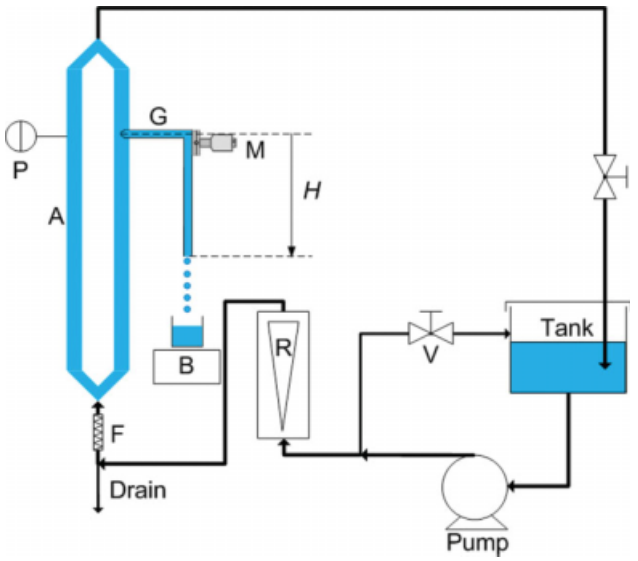

Figure 3. Schematic of flow FDG apparatus, where the flow in the annulus is turbulent (14,200 < $Re_{annulus}$ < 31,300).

A, annular test section; B, electronic balance; V, flow control valve; F, filter; G, gauging tube; H, hydrostatic head; M, micrometer; P, gauge pressure sensor; R, rotameter. [Color figure can be viewed in the online issue, which is available at www.interscience.wiley.com.]

CFD Simulations

Governing equations

CFD is employed to model the fluid flow in the (three-dimensional) quasi-static FDG configuration, using the finite element method (FEM) implemented in the commercial software COMSOL MULTIPHYSICS™ (version 3.4, Chemical Engineering Module). The governing continuity and incompressible, steady-state Navier-Stokes equations for a Newtonian liquid are

$$\text{Continuity:} \quad \nabla \cdot \mathbf{v} = 0 \quad (4)$$

$$\text{Navier-Stokes:} \quad \rho\mathbf{v} \cdot \nabla\mathbf{v} = -\nabla p + \mu\nabla^2\mathbf{v} + \rho g \quad (5)$$

where $\mathbf{v}$ is the velocity vector, p the pressure, ρ the density, μ the dynamic viscosity, and g the acceleration due to gravity, set to zero in this case for computational convenience.[22]

Physical properties such as density and viscosity were set constant throughout the entire system. All flows are laminar.

Model set-up and boundary conditions

The geometry of the model and the Cartesian coordinate axes employed are illustrated in Figure 4. A gauging nozzle is positioned with its axis perpendicular to the longitudinal axis of the annulus. Only a quarter of the annulus and half of the tube are modeled due to symmetry along the y-z plane for the tube and both the x-z and y-z planes for the annulus. The length of the annulus in the model is shorter than the true length of the test section to save computing time. The process fluid enters the annulus in the z-direction, crossing the top plane at $z = 0$, and leaves through the gauging tube in the y-direction, where $y = 0$ corresponds to the line along the convex surface that passes through the intersection of the projected center line of the gauging tube with that surface.

The quantitative information specified for each simulation is the velocity at the annulus top, the velocity profile at the tube outlet and the pressure at the annulus base. The simulated pressure drop across the nozzle, $\Delta p_{1'3'}$, is estimated as follows:

$$\Delta p_{1'3'} = p_{4'} - p_{1'} - \frac{128}{\pi}\frac{l'}{d^4}\frac{\mu}{\rho}m \quad (6)$$

where $p_{4'}$ and $p_{1'}$ are the computed pressures at the tube outlet and the bottom plane of the annulus, respectively. The final term on the right hand side of Eq. (6) is the Hagen-Poiseuille equation for pressure drop in the gauging tube due to friction, where l' is the length of the tube used in the simulations.

Once $\Delta p_{1'3'}$ is evaluated, the nozzle discharge coefficient, C_d, is calculated from Eq. (1) and compared with experimental C_d values.

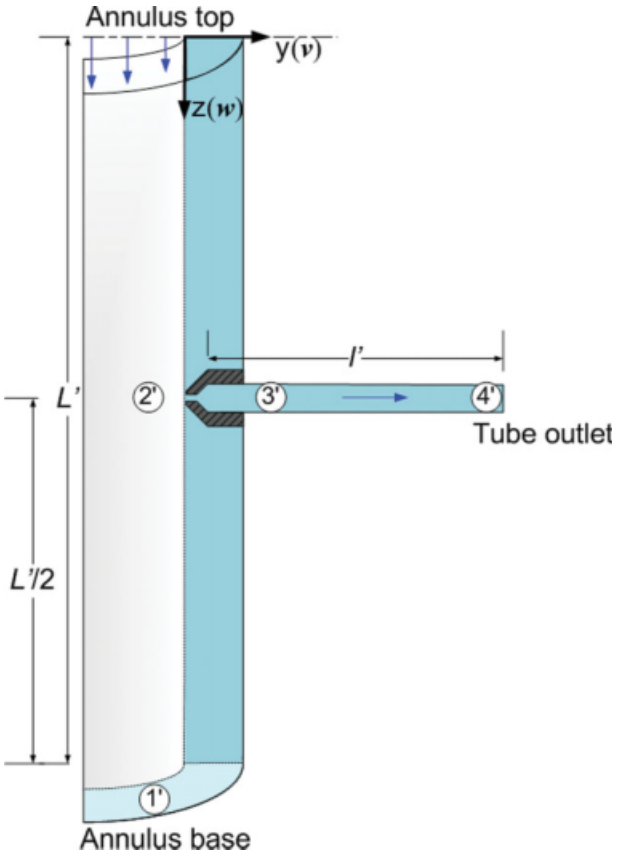

Figure 4. Simulation geometry.

Numbers refer to the stations in the simulation. The arrows indicate the entry flow in the annulus, and the exit flow in the tube. Coordinates: z, vertical (annulus) axis; y, horizontal (gauging tube) axis. Velocity components w and v are indicated. [Color figure can be viewed in the online issue, which is available at www.interscience.wiley.com.]

The boundary conditions imposed are:

(i) Annulus top, $z = 0$

A uniform z-wise velocity is specified at the annulus top, $\overline{w}_{\text{annulus}}$. This is a small flow required to balance the gauging flow leaving the system.

$$|\overline{w}_{\text{annulus}}| = |\overline{v}_{\text{tube}}| \frac{d^2}{D_h^2} \tag{7}$$

where $\overline{w}$ is the mean z-wise velocity. The x-wise and y-wise velocities u and v are set to zero at the top. In the simulation, it was assumed that the entry flow is in the z-direction only.

(ii) Gauging tube outlet, $y = l'$

Fully developed laminar flow is assumed, giving the Hagen-Poiseuille velocity profile

$$v = v_{\max}\left(1 - \left(\frac{r}{R}\right)^2\right) \tag{8}$$

where r is the radial coordinate measured from the tube center line, R is the inner radius of the tube, and $v_{\max}$ is the y-wise velocity at the tube center line, being twice the mean velocity calculated from experimental data, i.e. $v = 2\overline{v}_{\text{tube}}$. The x-wise and z-wise velocities u and w are set to zero. The length of the tube used in the simulations is that found by numerical trial and error to ensure that the flow at the tube outlet becomes fully developed; it varies with Re_{tube}, Re_{annulus} and h/d_t, with typically $25 < l'/d_t < 75$. For example, for the case $h/d_t = 0.06$, the model tube length to diameter ratio, l'/d_t, was increased from 50 to 100 and 125, all else being constant. The results revealed less than 0.5% difference in the values of the discharge coefficient, C_d. Thus, $l'/d_t = 50$ was deemed sufficient.

(iii) Annulus base, $z = L'$

The velocities u, v and w are all set to zero at this plane. The length of the annulus in the model, L', (shown in Figure 4) is determined by numerical trial and error, i.e. varying the ratio $L'/D_h \sim 7$, 10, and 16 (for the specific case $h/d_t = 0.06$). The results showed less than 0.1% difference in the values of the discharge coefficient, C_d. Hence, $L'/D_h \sim 7$ was chosen for all simulations. The pressure at the base is set to the (negative) pressure of the hydrostatic head pressing down on the fluid, viz.

$$p_{1'} = \rho g\left(H' + \frac{L'}{2}\right) \tag{9}$$

where H' is the height of the liquid in the test section above the gauge (Figure 2).

(iv) Walls

The walls of the annulus, the gauge, the nozzle, and lip of the nozzle are all modeled as impermeable and free of slip (normal and tangential components of the velocity are zero).

(v) Symmetry

There is no flow across the y-z and x-z planes of symmetry, thus

$$\mathbf{n}\cdot v = 0 \tag{10}$$

where $\mathbf{n}$ is the normal vector of the relevant plane.

Meshing and convergence

The grids used in the simulation were generated using the internal mesh generator in COMSOL MULTIPHYSICS. The domain was represented using tetrahedral elements. A preliminary simulation was run, and the flow field obtained. This demonstrated where velocity and pressure gradients were high. A higher concentration of elements is assigned to the clearance region beneath the nozzle where the steepest velocity and pressure gradients exist, so the mesh was refined to obtain satisfactory resolution there. The size of the elements at the nozzle region was set to ~5% of the size of the elements in the rest of the domain. Figure 5 shows a typical example of the refined mesh. The number of elements required to achieve convergence varied with h/d_t, l'/d, L'/D and Re_{tube}. To optimize the number of elements it was necessary to carry out a mesh-independence study; this was done by performing a number of simulations with different mesh sizes, starting from a coarse mesh and refining it until results were no more dependent on the mesh size.

A satisfactory solution took ~17 min to compute, on a desktop PC with a 3.16 GHz dual core processor and 3.33 GB RAM. Convergence was tested by comparing the values

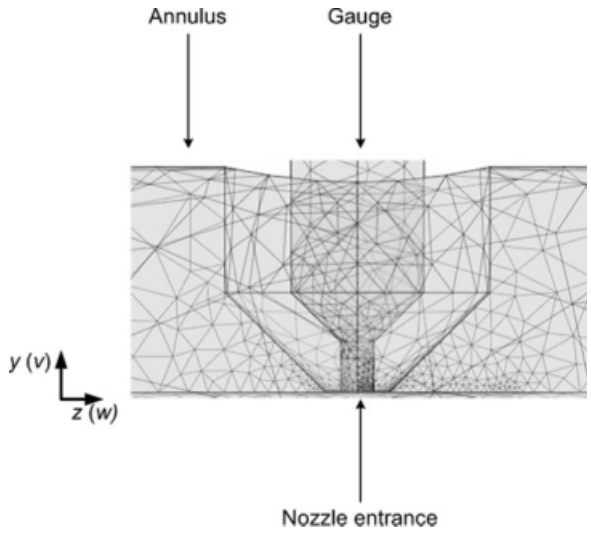

Figure 5. Projection of the FEM meshing for H = 640 mm, h/d_t = 0.04, l'/d_t = 25 in the nozzle region.

The dark section beneath the nozzle denotes a high concentration of meshing.

of velocity and pressure from successive iterations; tolerances were set at 10^{-6} m/s (vs. a lowest radial mean velocity in the gauging tube of 3×10^{-3} m/s) or 10^{-6} Pa (vs. a lowest reference pressure of -1815 Pa), for the velocity and pressure, respectively. The tolerance dictates the error in each integration step. Numerical accuracy was confirmed via conservation of mass, i.e. the mass flowing into the system minus the mass flowing out should equal zero. The numerical model gives an error of less than 4% for all cases investigated, with a maximum flow of 1.9×10^{-3} kg/s.

Results and Discussion

Flow behavior in the quasi-static case

For the static-FDG experiments, the CFD simulation of the velocity component in the direction of the tube axis for $H = 640$ mm in the range $h/d_t = 0.04$ to 0.40 ($Re_{tube} = 60$–557) is shown in Figure 6. The highest velocity occurs within the throat of the nozzle with expansion further up in the tube. The flow in the nozzle and tube is symmetrical. As the clearance, and hence Re_{tube} increases, a longer gauging tube is required to achieve the well developed velocity profile in the tube for the numerical model to converge, with $l'/d_t = 75$ for the highest case of Re_{tube} investigated ($Re_{tube} = 577$).

Comparisons of nozzle discharge coefficient in the quasi-static case: Experiments and CFD

In the experiment, the hydrostatic head driving the gauging flow, H, is set, the clearance, h, fixed, and the mass flow rate, m, is measured to calculate the Reynolds number at the gauging tube outlet, Re_{tube}. In the CFD simulations, the clearance and mass flow rates are fixed and set equal to the experimental values. The value of the pressure drop at the

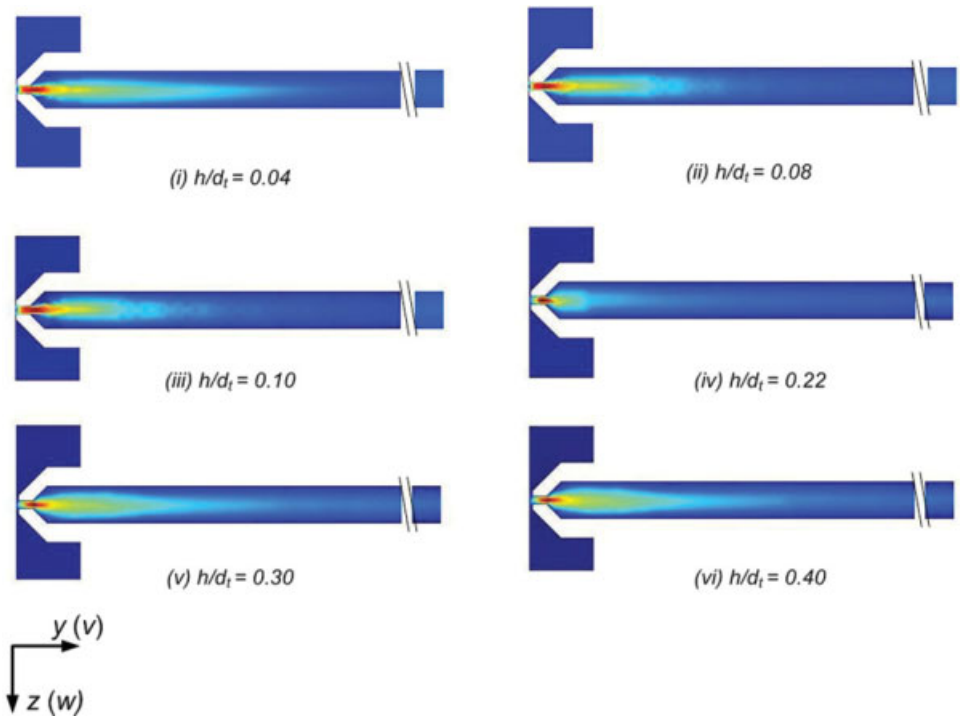

Figure 6. Horizontal (y-wise) velocity component in the tube at the y-z plane of symmetry for H = 640 mm, p_s = 2305 Pa.

(i) $h/d_t = 0.04$, $Re_{tube} = 60$; (ii) $h/d_t = 0.08$, $Re_{tube} = 142$; (iii) $h/d_t = 0.10$, $Re_{tube} = 210$; (iv) $h/d_t = 0.22$, $Re_{tube} = 446$; (v) $h/d_t = 0.30$, $Re_{tube} = 514$; (vi) $h/d_t = 0.40$, $Re_{tube} = 557$. Red color indicates highest y-wise velocity and blue color lowest value. [Color figure can be viewed in the online issue, which is available at www.interscience.wiley.com.]

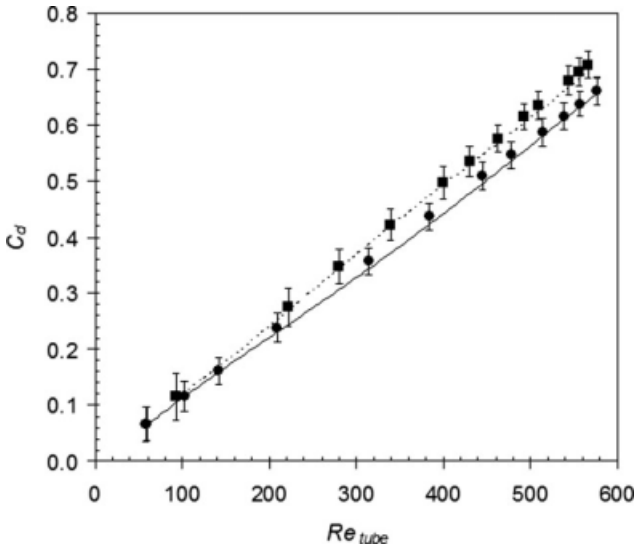

Figure 7. Comparison of experimental and simulated C_d values for quasi-static FDG.

Symbols, experimental data; squares, $H = 540$ mm; circles, $H = 640$ mm. Lines, loci interpolated from CFD results; dashed line, $H = 540$ mm; solid line, $H = 640$ mm.

tube outlet is computed, and $\Delta p_{1'3'}$ is evaluated via Eq. (6) and subsequently employed to calculate C_d via Eq. (1).

The experimental C_d values and those estimated from the numerical model are compared in Figure 7, for $H = 540$ and 640 mm for the quasi-static FDG in the range $0.04 < h/d_t < 0.60$. The loci plotted for the simulation results are obtained by interpolation. The agreement between the CFD predictions and the experimental values is satisfactory, to 4% approximately, and lie within the bounds of experimental error, thereby suggesting that the assumptions made in the model are adequate.

Stresses on the gauged surfaces in the quasi-static case

It is desirable to calculate both the shear and normal (suction) stresses generated by the gauging flow, as these have been demonstrated to have a significant effect on the removal of fouling deposits.[4,23] The stresses acting on the gauged surface can be readily calculated from the simulated velocity field.

The distribution of the normal stress on the inner convex surface of the annulus in the z-direction, directly underneath the nozzle (Figure 8a shows a sketch of the location), for $H = 640$ mm is shown in Figure 8b. Consider the straight line along the convex surface that passes through the intersection of the projection of the tube center line with the surface. The coordinate z measures the distance along that line from that intercept: $z = z' - L'/2$. The normal (suction) stress is high within the throat of the nozzle ($0 \le z' \le 0.5$ mm) and decays to a small value at $z' > 1$ mm. For small clearances, $h/d_t = 0.06$–0.10, the suction stress peaks at the position of the inner rim of the nozzle ($z' = 0.5$ mm), in agreement with previous results of Chew et al.[23] Figure 8b reveals that the z-wise shear stress is approximately zero at the center line of the tube ($z' = 0$), reaches a maximum beneath the nozzle lip ($z' = 0.5$–1.0 mm) and approaches zero asymptotically for $z' > 1$ mm. The magnitude of the z-wise shear stress at a given value of z' decreases as the gauge is moved away from inner surface, with the peak value decreasing from 42 Pa ($h/d_t = 0.06$) to 3 Pa ($h/d_t = 0.18$). When the gauge is moved further away, the effect of the z-wise shear stress and normal (suction) stress on the surface of the annulus becomes negligible (approximately zero for $h/d_t = 0.30$).

The components of the stress tensor acting around the circumference, a, of the inner cylinder in both the y-direction (τ_{zy}) and the x-direction (τ_{zx}) can be evaluated from the simulation. In the region beneath the gauging nozzle, these two shear stress components can be combined to evaluate the shear stress around the circumference of the inner cylinder, τ_{za}, as follows:

$$\tau_{za} = \sqrt{\tau_{zy}^2 + \tau_{zx}^2} \tag{11}$$

The gap between the gauging nozzle and the inner surface increases as one moves around the circumference of the inner cylinder away from the plane in Figure 8. The change in shear stress acting on the surface is presented in Figure 9. The abscissa is the arc length, a, around the circumference of the inner cylinder. The highest values of shear stress around the circumference of the inner cylinder occur within the throat and underneath the nozzle rim. The peak shear stress (τ_{za}), for all cases of h/d_t, is smaller than that acting in the z-direction ($\tau_{yz'}$), demonstrating the effect of a curved surface. For all cases considered, the peak shear stress occurs close to the inner rim of the nozzle. These results are consistent with the experimental observations of Tuladhar et

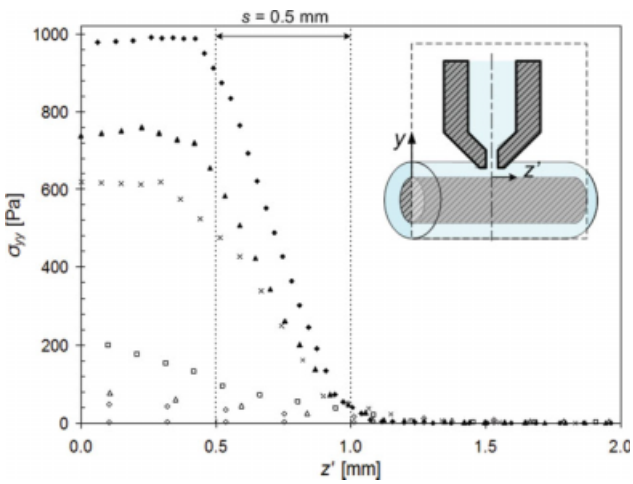

Figure 8. Normal (suction) stress (σ_{yy}), and shear stress ($\tau_{yz'}$) imposed by the gauging flow on the inner convex surface of the annulus (at $y = 0$), directly beneath the gauge, as a function of the annulus axial coordinate measured from the gauge central axis, as shown on the inset.

Conditions: $H = 640$ mm, $p_s = 2305$ Pa. Symbols: solid diamonds, $h/d_t = 0.06$, $Re_{tube} = 102$; solid triangles, $h/d_t = 0.08$, $Re_{tube} = 142$; crosses, $h/d_t = 0.10$, $Re_{tube} = 210$; open squares, $h/d_t = 0.14$, $Re_{tube} = 314$; open triangles, $h/d_t = 0.18$, $Re_{tube} = 383$; open diamonds, $h/d_t = 0.22$, $Re_{tube} = 446$. $h/d_t = 0.22$, $h/d_t = 0.30$, $h/d_t = 0.40$. [Color figure can be viewed in the online issue, which is available at www.interscience.wiley.com.]

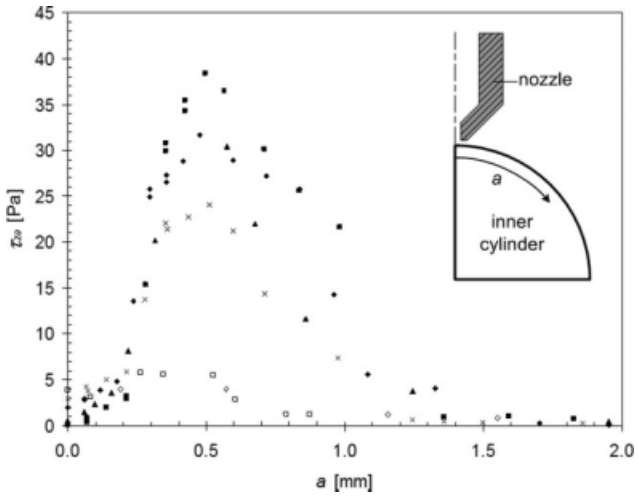

Figure 9. Shear stress imposed by the gauging flow on the convex surface at different positions along the arc, as shown in the inset.

Conditions: $H = 640$ mm, $p_s = 2305$ Pa. Symbols: solid squares, $h/d_t = 0.04$, $Re_{tube} = 60$; solid diamonds, $h/d_t = 0.06$, $Re_{tube} = 102$; triangles, $h/d_t = 0.08$, $Re_{tube} = 142$; crosses, $h/d_t = 0.10$, $Re_{tube} = 210$; open squares, $h/d_t = 0.14$, $Re_{tube} = 314$; open triangles, $h/d_t = 0.18$, $Re_{tube} = 383$; open diamonds, $h/d_t = 0.22$, $Re_{tube} = 446$.

al.[4] and Chew et al.,[23] who noted that deposit distortion was usually located under the rim of the nozzle. The magnitude of the peak shear stresses in both cases is noteworthy. The equivalent mean velocities, $\overline{w}_{annulus}$, for turbulent flow conditions in an annulus can be estimated from

$$\overline{w}_{annulus} = \sqrt{\frac{2\tau_{yz'}}{\rho C_f}} \tag{12}$$

where the Fanning friction factor, C_f, is estimated using the Davis correlation for annular geometry,[24] valid for $3000 < Re_{annulus} < 10^6$.

$$C_f\left(\frac{D_o/D_i - 1}{D_o/D_i}\right)^{-0.1} = 0.055 Re_{annulus}^{-0.2} \tag{13}$$

where D_o and D_i are the outer and inner diameter of the annulus, respectively.

The estimated mean velocities for turbulent flows of water in an annulus that would produce a wall shear stress of magnitude corresponding to the maximum radial shear stress in FDG lie in the range 0.6 m/s $< \overline{w}_{annulus} <$ 3.9 m/s. These values are comparable to the range of mean pipe velocities suggested for cleaning-in-place installations (1–3 m/s) by Timperley,[25] although more modern work tends to recommend values of wall shear stress or Reynolds number. It is noteworthy that gauging under readily obtainable laboratory conditions could therefore replicate the mean shear stress values observed in turbulent liquid flows.

Gauging in turbulent annular flow

In this section, only experimental data are presented. The gauging discharge flow rate, m, as a function of h/d_t, obtained for $Re_{annulus}$ values in the turbulent flow regime is plotted in Figure 10. The discharge mass profiles are similar for both nozzle advancing and retreating modes. The discharge flow rate increases with $Re_{annulus}$ due to the associated increase in the static gauge pressure. The profiles exhibit three zones. The first zone is described as the "curvature zone" at $0 < h/d_t < 0.1$, where the mass flow rate remains constant, independent of the gauge position. This is due to the geometry of the system; there is always a gap for liquid to flow into the gauge even when it is in contact with the gauged surface ($h/d_t = 0$). The second zone is labeled the "incremental zone," between $0.1 < h/d_t < 0.4$, where the flow increases almost linearly with increasing clearance; this is the "useful working range" of the instrument, to be exploited for thickness measurement. The third zone, at $h/d_t > 0.4$, is labeled the "asymptotic zone," as the mass flow rate is relatively insensitive to the clearance. With the exception of the initial curvature zone, the behavior of the gauge in the annular geometry and the resulting discharge mass profile resembles that reported previously for flat surfaces,[2] employing the same nozzle design (d_t, s, λ, α). The only difference is the wall thickness of the gauging tube, k, which is 2 mm in this investigation and was 1 mm for Tuladhar's experiments.

The effect of clearance on nozzle discharge coefficient, C_d, is plotted in Figure 11 for $14{,}200 \leq Re_{annulus} \leq 31{,}300$. Data are reported for the nozzle advancing mode. All C_d profiles display an initial flat region followed by an increase toward an asymptotic value, reached around $h/d_t = 0.5$.

Buffer sublayer

It is instructive to compare the gauging length scale with the characteristic length scales of the flow regime in the

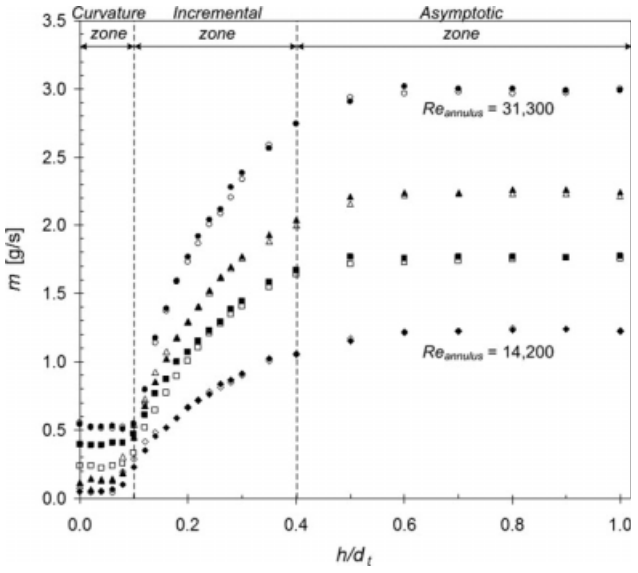

Figure 10. Effect of $Re_{annulus}$ on experimental FDG discharge profiles obtained for $H = 405$ mm.

Symbols: circles, $Re_{annulus} = 31{,}300$, $p_s = 42{,}000$ Pa; triangles, $Re_{annulus} = 22{,}800$, $p_s = 28{,}000$ Pa; squares, $Re_{annulus} = 19{,}900$, $p_s = 24{,}800$ Pa; diamonds, $Re_{annulus} = 14{,}200$, $p_s = 19{,}600$ Pa. Solid symbols represent the gauge operating in advancing mode and open symbols represent the gauge operating in retreating mode. Data reproducibility is evident in the "incremental" and "asymptotic" zone for all cases investigated.

annulus. The interaction between the gauging flows and the slower moving fluid near the wall of the inner cylinder was considered, albeit approximately, using the universal velocity profile to estimate the boundaries of the viscous ($\delta^+ = 5$) and buffer sublayers ($\delta^+ = 40$) for the inner portion of the annular velocity profile. Knudsen and Katz[24] state the following relationship for δ^+, valid for $Re_{\text{annulus}} < 7 \times 10^5$:

$$\delta^+ = \overline{w}_{\text{annulus}} \frac{\delta\rho}{\mu} \sqrt{\frac{C_f}{2}} \tag{14}$$

where δ is the distance from the surface of the inner cylinder and δ^+ is the friction distance. Most texts refer to these quantities as y and y^+, but we employ δ and δ^+ to avoid confusion with the Cartesian coordinate used in the simulation.

The viscous and buffer sublayer thickness estimations are plotted in Figure 12. For the useful operating range, the nozzle tip operates within the buffer sublayer ($0.10 < h/d_t < 0.40$), although at higher Re_{annulus} the operating range may extend into the core region. The latter aspect is subject to considerable uncertainty, as the accuracy of the estimate is low owing to the uncertainty in the C_f correlation, the effect of the obstruction that the nozzle presents to the flow in the annulus, and the effect of the gauging flow itself. Nevertheless, the estimates indicate that gauging operates within the curvature region of the flow, where viscous effects are important.

Potential application of FDG to annular flow systems

FDG has been demonstrated here to work well for curved surfaces, and specifically the inner surface of the annular flow configuration that is widely employed for laboratory studies of heat exchanger fouling and cleaning (Table 1). The technique has been shown to be suitable for real-time monitoring of deposit thickness in the turbulent regime, where many industrially important tests are operated. Lower

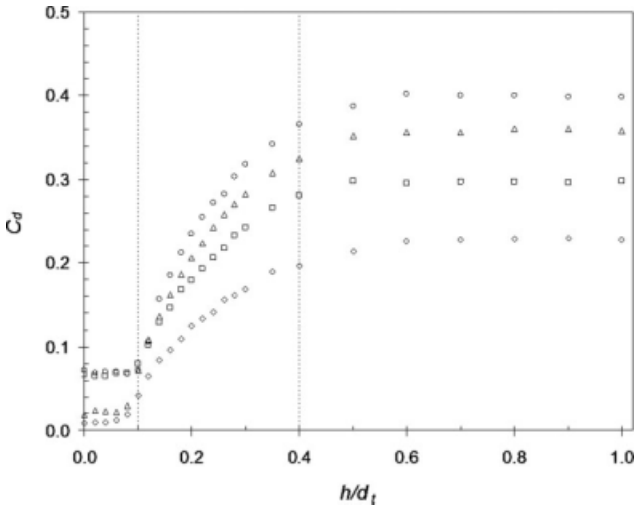

Figure 11. Nozzle discharge coefficient, C_d, vs. clearance, h/d_t, obtained for H = 405 mm.

Data for nozzle advancing mode. Symbols: circles, $Re_{\text{annulus}} = 31{,}300$, $p_s = 42{,}000$ Pa; triangles, $Re_{\text{annulus}} = 22{,}800$, $p_s = 28{,}000$ Pa; squares, $Re_{\text{annulus}} = 19\,900$, $p_s = 24{,}800$ Pa; diamonds, $Re_{\text{annulus}} = 14{,}200$, $p_s = 19{,}600$ Pa.

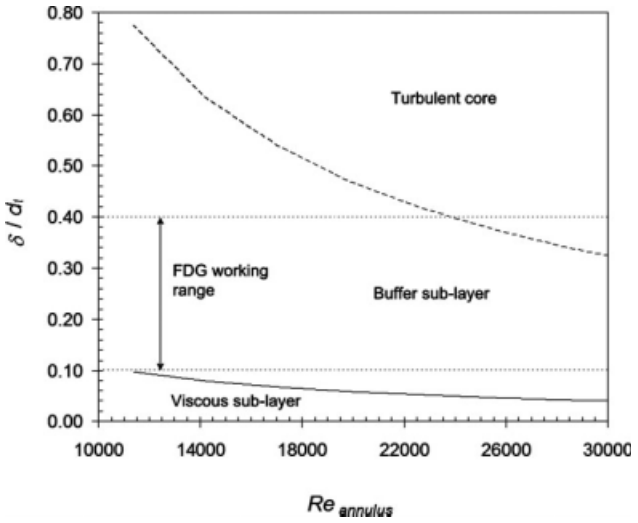

Figure 12. Estimated viscous sublayer and buffer sublayer thickness ratio for the geometry employed in these experiments.

The dashed horizontal lines indicate the working range of the gauge.

velocities (i.e. in the laminar regime) were not considered in this work but extension of the technique to this regime is considered straightforward, given that the gauge behavior in the turbulent regime is rather similar to that in the quasi-static regime (where there is no net advective flow and the experimental results agree with CFD simulations closely), and the technique has already been demonstrated to work on duct flows with flat surfaces in the laminar regime.[19] Installing a gauge on an annular fouling probe may now be expected to generate new information about the deposit layers. Clearance-time data can be generated to track the thickness of deposits, and those thicknesses could be compared with the thicknesses estimated indirectly from pressure drop measurements; differences can be related to deposit surface roughness. The thermal resistance of deposits is often measured via heat transfer measurements; combining this property with deposit thickness will yield estimates of thermal conductivity, as described by Tuladhar et al.[26] in their study of whey protein fouling on flat plates. Finally, if the flow can be stopped for a short period, the quasi-stagnant mode of operation can be used to assess the strength of the fouling deposit. Similar arguments can be applied to cleaning studies.

Conclusions

The present work has demonstrated that the technique of FDG can work effectively for a curved surface; specifically, in an annular geometry. Experiments in the turbulent regime revealed three characteristic zones, namely "curvature," "incremental," and "asymptotic," of which the "curvature" zone is new to the current (curved) geometry. The effective working range of the gauge is between 0.1 and 0.4 h/d_t. Moreover, measurements and CFD calculations carried out for the quasi-static case showed an agreement to 4% or better for all experiments.

Acknowledgments

Financial support from the Engineering and Physical Sciences Research Council (EPSRC EP/D50306X) is gratefully acknowledged, as is Royal Academy of Engineering Research Fellowship for Y. M. J. Chew. Dr. M. Abubakar and G. Chapman made several invaluable contributions in the design and construction of the apparatus.

Notation

a = arc length along annulus cross section, m
C_{cur} = coefficient of hydraulic friction of a curved bend, dimensionless
C_d = discharge coefficient accounting for nozzle flow complexity and energy loss, dimensionless
C_f = fanning friction factor, dimensionless
d = inner diameter of dynamic gauging tube, m
d_t = nozzle throat diameter, m
D_h = hydraulic diameter of the annulus, m
D_i = inner diameter of the annulus, m
D_o = outer diameter of the annulus, m
g = acceleration due to gravity, m/s^2
h = clearance between nozzle tip and gauging surface, m
H = hydrostatic head providing pressure driving force for gauging flow, m
H' = height of liquid in the test section above the gauge, m
k = wall thickness of gauging tube, m
K = loss coefficient in tube for 90° bend, dimensionless
L = length of annular test section, m
L' = computational fluid dynamics model of duct length, m
l = length of siphon tube, m
l' = computational fluid dynamics model of tube length, m
m = tube discharge mass flow rate, kg/s
$\mathbf{n}$ = normal vector
p = pressure, Pa
r = radial coordinate of the gauging nozzle, m
R = inner radius of the gauging tube or radius of the bend in the gauging tube, m
Re = Reynolds number, dimensionless
s = width of nozzle rim, m
u = x-wise velocity, m/s
$\mathbf{v}$ = velocity vector
v = y-wise velocity, m/s
$\bar{v}$ = mean y-wise velocity, m/s
w = z-wise velocity, m/s
$\bar{w}$ = mean z-wise velocity, m/s
x = coordinate
y = coordinate
z = coordinate

Greek letters

α = nozzle inner angle, °
α_{bend} = angle of the bend, °
δ = distance from the surface of the inner cylinder, m
δ^+ = dimensionless thickness ratio
λ = length of nozzle exit, m
μ = dynamic viscosity, Pa s
σ_{yy} = normal stress, Pa
ρ = density, kg/m^3
$\tau_{yz'}$ = shear stress on the y-plane in the z-direction, Pa
τ_{zx} = shear stress on the z-plane in the x-direction, Pa
τ_{zy} = shear stress on the z-plane in the y-direction, Pa
τ_{za} = shear stress on the z-plane in the a-direction, Pa

Subscripts

actual = actual
annulus = annulus
bend = bend
cur = curved
eff = effective
h = hydraulic
i = inner
ideal = ideal
max = maximum
o = outer
s = static
total = total
tube = tube

Abbreviations

CFD = computational fluid dynamics
FDG = fluid dynamic gauging
FEM = finite element method
HLPS = hot liquid process simulator
HTRI = heat transfer research incorporated
HTFU = high temperature fouling unit
PFRU = portable fouling research unit

Literature Cited

1. ESDU (Engineering Sciences Data Unit). Fouling in cooling systems using fresh water. Data Item 08002. London, U.K.: ESDU Intl., 2008.
2. Tuladhar TR, Paterson WR, Macleod N, Wilson DI. Development of a novel non-contact proximity gauge for thickness measurement of soft deposits and its application in fouling studies. *Can J Chem Eng*. 2000;78:935–947.
3. Saikhwan P, Chew YMJ, Paterson WR, Wilson DI. Fluid dynamic gauging: a technique for studying the cleaning of food process surfaces. *Food Manuf Efficiency*. 2007;1:34–41.
4. Tuladhar TR, Paterson WR, Wilson DI. Dynamic gauging in duct flows. *Can J Chem Eng*. 2003;81:279–284.
5. Hooper RJ, Liu W, Fryer PJ, Paterson WR, Wilson DI, Zhang Z. Comparative studies of fluid dynamic gauging and a micromanipulation probe for strength measurements. *Food Bioprod Process*. 2006;84:353–358.
6. Bennett CA, Kistler RS, Nangia K, Al-Ghawas W, Al-Hajji N, Al-Jemaz A. Observation of an isokinetic temperature and compensation effect for high temperature crude oil fouling. In: *ECI Conference on Heat Exchanger Fouling and Cleaning*, Tomar, Portugal, 2007. http://services.bepress.com/eci/heatexchanger2007/
7. Oufer L. *Fouling Characteristics of Organic Fluids*. Ph.D. thesis, Oregon State University, Corvallis, OR, 1990.
8. Chen YC, Quan ZH, Ma CF. Investigation of fouling process for convective heat transfer in an annular duct. In: *ECI Conference on Heat Exchanger Fouling and Cleaning*, Tomar, Portugal, 2007. Available at http://services.bepress.com/eci/heatexchanger2007/
9. Knudsen JG, Hays GF. Simulation of fouling in heat exchangers using an annular test section. In: *Proceedings of an International Conference on Mitigation of Heat Exchanger Fouling and its Economic and Environmental Implications*, Banff, Alberta, Canada, 1999.
10. Augustin W, Bohnet M. Influence of the ratio of free hydrogen ions on crystallisation fouling. *J Chem Eng Process*. 1995;34:79–85.
11. Toma P, Ivory J, Korpany G, deRocco M, Holloway L, Goss C, Ibrahim J, Omar I. A two-layer paraffin deposition structure observed and used to explain the removal and aging of paraffin deposits in wells and pipelines. *J Energy Resour Technol*. 2006;128:49–61.
12. Hays GF, Beardwood ES, Colby SJ. Enhanced heat exchanger tubes: their fouling tendancy and potential cleanup. In: *ECI Conference on Heat Exchanger Fouling and Cleaning—Challenges and Opportunities*, Kloster Irsee, Germany, 2005. Available at http://services.bepress.com/eci/heatexchanger2005/
13. Bansal B, Chen XD, Lin SXQ. Skim milk fouling during ohmic heating. In: *ECI Conference on Heat Exchanger Fouling and Cleaning—Challenges and Opportunities*, Kloster Irsee, Germany, 2005. Available at http://services.bepress.com/eci/heatexchanger2005/
14. Isogai S, Nakamura M. Fouling mitigation of a reboiler by optimization of additive and operating conditions. In: *ECI Conference on Heat Exchanger Fouling and Cleaning—Challenges and Opportunities*, Kloster Irsee, Germany, 2005. Available at http://services.bepress.com/eci/heatexchanger2005/
15. Bode K, Hooper RJ, Augustin W, Paterson WR, Wilson DI, Scholl S. Pulsed flow cleaning of whey protein fouling layers. *Heat Transfer Eng*. 2007;28:202–209.

16. Waktinson AP. Comparison of crude oil fouling using two different probes. In: *ECI Conference on Heat Exchanger Fouling and Cleaning: Fundamentals and Applications*, Santa Fe, New Mexico, USA, 2003. Available at http://services.bepress.com/eci/heatexchanger/
17. Tijing LD, Pak BC, Baek BJ, Lee DH, Kim CS, Cho YI. Use of catalytic alloys for physical water treatment technology to mitigate mineral fouling in heat exchangers. In: *ECI Conference on Heat Exchanger Fouling and Cleaning*, Tomar, Portugal, 2007 http://services.bepress.com/eci/heatexchanger2007/.
18. Jennings DW, Weispfennig K. Effects of shear and temperature on wax deposition: coldfinger investigation with a Gulf of Mexico crude oil. *Energy Fuels*. 2005;19:1376–1386.
19. Gu T, Chew JYM, Paterson WR, Wilson DI. Experimental and CFD studies of fluid dynamic gauging in duct flows. *Chem Eng Sci*. In press.
20. Idelchik IE. *Handbook of Hydraulic Resistance*, 3rd ed. Florida: CRC Press, 1994:336–359.
21. Baker DK, Vliet GC, Lawler DF. Experimental apparatus to investigate calcium carbonate scale growth rates. In: *Proceedings of an International Conference on Mitigation of Heat Exchanger Fouling and its Economic and Environmental Implications*, Banff, Alberta, Canada, 1999.
22. Tritton DJ. *Physical Fluid Dynamics, 2nd ed*. Oxford, U.K.: Oxford University Press, 1988:58–59.
23. Chew JYM, Paterson WR, Wilson DI. Fluid dynamic gauging for measuring the strength of soft deposits. *J Food Eng*. 2004;65:175–187.
24. Knudsen JG, Katz DL. *Fluid Dynamics and Heat Transfer*. New York: McGraw-Hill, 1958:190–198.
25. Timperley DA. Cleaning in place. *J Dairy Technol*. 1989;42:32–33.
26. Tuladhar TR, Paterson WR, Wilson DI. Thermal conductivity of whey protein undergoing swelling. Measurement by dynamic gauging. *Food Bioprod Process*. 2002;80:332–339.
27. The Engineering ToolBox 2005. Available at http://www.engineeringtoolbox.com/surface-roughness-ventilation-ducts-d_209.html (accessed October 8, 2008).

Appendix

Derivation of effective tube length, l_{eff}

The total pressure drop in the gauging tube equals the losses in the 90° bend plus the frictional losses due to the tube wall:

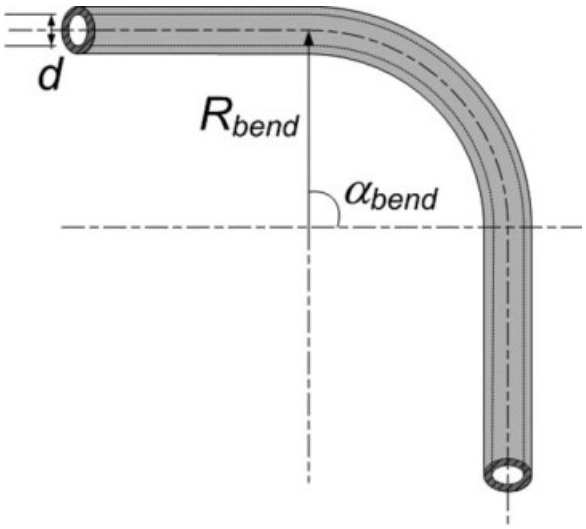

Figure A1. Schematic of a circular pipe with a 90° bend.

$$\Delta p_{\text{total}} = \Delta p_{\text{bend}} + \Delta p_{\text{wall}}$$

where

$$\Delta p_{\text{total}} = m\left(\frac{128}{\pi}\frac{l_{\text{eff}}}{d^4}\frac{\mu}{\rho}\right)$$

$$\Delta p_{\text{bend}} = K\left(\frac{1}{2}\rho v_{\text{tube}}^2\right)$$

$$\Delta p_{\text{wall}} = m\left(\frac{128}{\pi}\frac{l}{d^4}\frac{\mu}{\rho}\right)$$

where m is the tube discharge mass flow rate, l_{eff} is the tube effective length, μ is the dynamic viscosity, ρ is the density of the fluid, d is the tube diameter, and K is the loss coefficient due to the 90° bend.

Hence,

$$m\left(\frac{128}{\pi}\frac{l_{\text{eff}}}{d^4}\frac{\mu}{\rho}\right) = K\left(\frac{1}{2}\rho v_{\text{tube}}^2\right) + m\left(\frac{128}{\pi}\frac{l}{d^4}\frac{\mu}{\rho}\right)$$

$$\therefore l_{\text{eff}} = l + K\left(\frac{\pi}{256}\frac{\rho^2}{\mu}\frac{v_{\text{tube}}^2}{m}d^4\right)$$

$$l_{\text{eff}} = l + K\left(\frac{\rho}{\mu}\frac{d^2}{64}\right)v_{\text{tube}}$$

The value of K is calculated as follows[20]:

$$K = 0.0175 C_{\text{cur}} \alpha_{\text{bend}} \frac{R_{\text{bend}}}{d}$$

where C_{cur} is the coefficient of hydraulic friction of a curved bend, α_{bend} is the angle of the bend in degrees, R_{bend} is the radius of the bend and d is the internal diameter of the tube (Figure A1). This equation is valid for smooth curved tubes made of glass, brass, lead, rubber, and steel, at relative roughness of less than 2×10^{-4} (the relative roughness of stainless steel is 1.5×10^{-5})[27] and a bend ratio of $R_{\text{bend}}/d \geq 3$ ($R_{\text{bend}}/d = 7$ for this case).

C_{cur} is a function of the tube Reynolds number, Re_{tube}, and the bend ratio, R_{bend}/d, viz.

$$\text{at } 50 < Re_{\text{tube}}\sqrt{\frac{d}{2R_{\text{bend}}}} < 600 \quad C_{\text{cur}} = \frac{20}{Re_{\text{tube}}^{0.65}}\left(\frac{d}{2R_{\text{bend}}}\right)^{0.175}$$

$$\text{at } 600 < Re_{\text{tube}}\sqrt{\frac{d}{2R_{\text{bend}}}} < 1400 \quad C_{\text{cur}} = \frac{10.4}{Re_{\text{tube}}^{0.55}}\left(\frac{d}{2R_{\text{bend}}}\right)^{0.225}$$

$$\text{at } 1400 < Re_{\text{tube}}\sqrt{\frac{d}{2R_{\text{bend}}}} < 5000 \quad C_{\text{cur}} = \frac{5}{Re_{\text{tube}}^{0.45}}\left(\frac{d}{2R_{\text{bend}}}\right)^{0.275}$$

Manuscript received July 31, 2008, and revision received Oct. 27, 2008.